

# Ring Artifacts Removal Based on Implicit Neural Representation of Sinogram Data

Ligen Shi, Xu Jiang, Yunze Liu, Chang Liu, Ping Yang, Shifeng Guo, and Xing Zhao\*

**Abstract**—Inconsistent responses of X-ray detector elements lead to stripe artifacts in the sinogram data, which manifest as ring artifacts in the reconstructed CT images, severely degrading image quality. This paper proposes a method for correcting stripe artifacts in the sinogram data. The proposed method leverages implicit neural representation (INR) to correct defective pixel response values using implicit continuous functions and simultaneously learns stripe features in the angular direction of the sinogram data. These two components are combined within an optimization constraint framework, achieving unsupervised iterative correction of stripe artifacts in the projection domain. Experimental results demonstrate that the proposed method significantly outperforms current state-of-the-art techniques in removing ring artifacts while maintaining the clarity of CT images.

**Index Terms**—Ring Artifact Removal, Implicit Neural Representation, Stripe Artifacts Separation

## I. INTRODUCTION

**R**ING artifacts are common artifacts in computed tomography (CT) imaging, primarily caused by inconsistent responses of detector elements to X-rays or damage to these elements [1], [2]. Photon Counting Detectors (PCDs), due to their photon energy discrimination capability, have the potential advantage of providing more imaging information compared to conventional CT detectors [3], [4]. However, their broader application is hindered by ring artifacts, as the detector elements are prone to damage. Inconsistent detector element responses lead to data deviations at different view angles, resulting in stripes in the sinogram. During CT image reconstruction, these stripes back-project as equidistant lines from the rotation center and, when accumulated from multiple view angles, form ring structures, known as ring artifacts.

Ligen Shi, Xu Jiang and Yunze Liu are with the School of Mathematical Sciences, Capital Normal University, Beijing 100048, China (e-mail: ligenshi0826@gmail.com; chianghsu97@gmail.com; 2220502075@cnu.edu.cn).

Ping Yang is with the Institute of Nuclear and New Energy Technology, Tsinghua University, Beijing 100084, China (e-mail: 2190501006@cnu.edu.cn).

Chang Liu is with the Institute of Applied Mathematics, Beijing Information Science and Technology University, Beijing 100101, China (e-mail: changliuct@gmail.com).

Shifeng Guo is with the Shenzhen Institute of Advanced Technology, Chinese Academy of Sciences, Shenzhen 518055, China (e-mail: sf.guo@siat.ac.cn).

Xing Zhao is with the school of Mathematical Sciences, Capital Normal University, Beijing, 100048, China (e-mail: zhaoxing\_1999@126.com).

Corresponding author: Xing Zhao

Removing these ring artifacts, or ring artifact correction, is a key technique for improving the quality of CT imaging.

Widely adopted methods for ring artifact removal include detector calibration methods [5]–[7], sinogram domain preprocessing methods [8]–[14], CT image post-processing methods [15]–[19], dual-domain iterative methods [20], [21], and data-driven methods [22]–[25]. Detector calibration includes dark-field correction, flat-field correction, and bad-pixel correction. However, equipment aging can lead to deviations in correction coefficients, making it difficult to completely remove ring artifacts by relying solely on detector calibration. To effectively remove these artifacts, detector calibration methods need to be combined with other methods to achieve better correction results. CT image post-processing methods involve Cartesian and polar coordinate transformations, potentially leading to a loss of image resolution. Dual-domain iterative methods leverage features from both the projection domain and the CT image domain to establish optimization functions through iterative solving. However, since the stripe artifacts in the sinogram represent high-frequency information, they manifest not only as ring artifacts in the reconstructed images but also spread throughout the image space, causing additional noise and artifacts. As shown in Fig. 1, (a) shows sinogram data without stripes, and (b) shows sinogram data with a single stripe. (c) and (d) show the FBP [26] reconstructions of (a) and (b), respectively. Comparing Fig. 1 (c) and Fig. 1 (d), besides the ring artifacts, Fig. 1 (d) also shows other noticeable artifacts. Therefore, it is challenging to achieve satisfactory results using single regularization constraints in the image domain. Data-driven supervised learning methods for artifact removal heavily depend on the size and quality of labeled datasets.

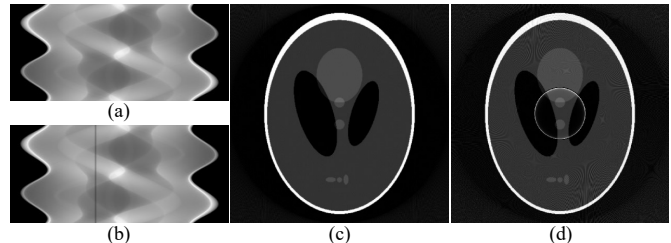


**Fig. 1.** (a) Sinogram data without stripes; (b) Sinogram data with one stripe artifact; (c) and (d) are the FBP-reconstructed CT images from (a) and (b), respectively.

For sinogram-domain preprocessing methods, they indi-

rectly eliminate ring artifacts in the reconstructed image by removing stripe artifacts in the sinogram. These methods directly leverage artifact features in the sinogram, avoiding potential information loss introduced during CT image reconstruction. However, existing sinogram-domain methods still face several challenges in stripe artifact removal, including: 1) loss of useful high-frequency information in the sinogram, resulting in blurry reconstructed CT images; 2) inaccuracies introduced when handling stripes caused by non-responsive detector elements with local interpolation; and 3) the lack of high-quality datasets, limiting the application of supervised learning methods.

To address these challenges, this paper proposes an unsupervised method for ring artifact removal based on the Implicit Neural Representation (INR) [27]–[30] of sinogram data. The proposed method effectively removes ring artifacts while preserving the details of reconstructed images, without the need for labeled datasets. The response of X-ray detector elements with inconsistent responses can be assumed as [20]:

$$I_m = C_m \cdot I_0 e^{-\int_L \mu(\mathbf{x}) dl}, \quad (1)$$

where  $C_m$  represents the gain factor between the measured count of the  $m$ -th detector element and the incident photon count, which is related to the response function of the detector element.  $I_0$  and  $I_m$  represent the number of received and emitted photons, respectively.  $\int_L \mu(\mathbf{x}) dl$  is the projection along path  $L$  containing  $C_m$  information. Eq. (1) can be rewritten as:

$$\int_L \mu(\mathbf{x}) dl = -\log(I_m/I_0) + \log(C_m), \quad (2)$$

where  $-\log(I_m/I_0)$  represents the ideal projection, and  $\log(C_m)$  corresponds to the stripe artifacts for the  $m$ -th detector element. Thus, the sinogram combines the Ideal Sinogram (IS) and Stripe Artifacts (SA).

As shown in Fig. 2, (a) is the sinogram with stripe artifacts, (b) is the IS, and (c) is the SA. Digital Radiography (DR) is primarily affected by scattering during the imaging process, resulting in low contrast while exhibiting local smoothness characteristics [31]. These properties of low contrast and local smoothness are well-suited for parameterization by neural networks [32], [33]. The inconsistent responses of detector elements to X-rays lead to substantial variations at the same scan view angle, resulting in noticeable stripes in the sinogram; nevertheless, local smoothness in IS is maintained in the detector direction. While the detector responses vary, the intensity fluctuations of X-rays received by the same detector element at adjacent view angles are minimal, resulting in sparse gradients in the angular direction. Inspired by the sorted sinogram method proposed in [14], the sorting of Figures 2 (a), (b), and (c) along the angular axis by the projection values results in Figures 2 (d), (e), and (f). Sorting significantly enhances the smoothness of IS in the detector direction and further emphasizes the sparsity of SA in the angular direction.

Based on this analysis, the sinogram is modeled as a combination of IS and SA, constructing a differentiable forward problem model. By incorporating the local smoothness of IS in the detector direction and the sparse distribution of SA in the

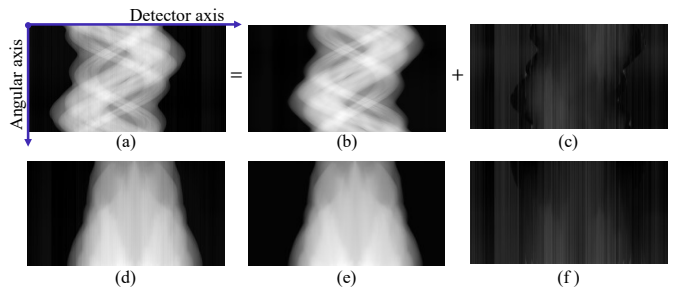


Fig. 2. (a) Sinogram data with stripe artifacts; (b) IS; (c) SA. (d), (e), and (f) are the sorted results of (a), (b), and (c) along the angular axis based on projection values. The display range is  $[0, 3.07]$  for (a), (b), (d), and (e), and  $[-0.5, 0.5]$  for (c) and (f). The Angular axis represents the angular direction, and the Detector axis represents the detector direction.

angular direction, we propose a unidirectional regularization framework that separates IS and SA.

The proposed method first classifies the pixels in the projection data into defective pixels (caused by non-responsive detector elements) and non-defective pixels (resulting from inconsistent X-ray detector responses). For non-defective pixels, the projection data is decomposed into the IS and SA under the unidirectional regularization framework, achieving the parameterization of IS from a “discrete-to-continuous” representation. For defective pixels, the implicit function fitted to the INR-parameterized IS is used for prediction, thereby avoiding inaccuracies introduced by local interpolation. Additionally, to avoid the loss of useful high-frequency information in the sinogram, a residual compensation strategy is employed to further enhance image details. The main contributions of this paper are as follows:

- 1) We propose an unsupervised method for stripe artifact removal, which eliminates stripe artifacts in the sinogram domain without relying on labeled datasets.
- 2) We leverage the continuous representation capability of INR-parameterized continuous functions to fit IS using data from non-defective pixels, enabling the prediction of projection values for defective pixels.
- 3) We introduce a unidirectional regularization framework for the effective separation of IS from SA. The regularizer  $\Psi_{IS}$  enforces local smoothness within IS, while  $\Psi_{SA}$  accentuates stripe features in SA and suppresses non-stripe artifacts, resulting in efficient separation of these two components.

## II. RELATED WORK

In the sinogram domain, methods for removing stripe artifacts can be further categorized into frequency and spatial domain filtering. Stripe artifacts manifest as high-frequency components in the frequency domain of the sinogram, making frequency domain filtering a commonly used method for their removal. For example, high-pass filtering [9] is used to correct projections by filtering out high-frequency components in the sinogram. Additionally, methods such as the variable window moving average and weighted moving average filters [10], as well as Butterworth low-pass filtering [11], are also employed. The combined wavelet-FFT filtering method [12] compresses

the stripe information into narrow bands and eliminates it by multiplying with a Gaussian damping function. While these methods can remove stripe artifacts to some extent, they often result in information loss in the projection, thereby reducing the quality of the reconstructed images.

Spatial domain filtering methods mainly use edge-preserving smoothing filters on the sinogram. The sorting-based method [14] removes stripe artifacts by applying median filtering to the sorted sinogram, while the combination-based method [14] identifies and interpolates the defective pixels through linear fitting, followed by filtering. For removing ring artifacts in PCD, Wu et al. [34] generated a mean vector by averaging multi-angle projection images, applied a TV- $L_1$  aG filter to smooth the mean vector, and compensated the filtered mean vector back into the sinogram to eliminate stripe artifacts. However, the effectiveness of these methods depends on the accurate localization and compensation of stripe artifacts.

In CT image post-processing, a common technique involves converting images from Cartesian to polar coordinates. This transformation turns ring artifacts into stripe-like artifacts that are easier to identify and address. After processing in polar coordinates, the image is converted back to Cartesian coordinates to remove the ring artifacts. For example, Sijbers et al. [15] use morphological operators to extract regions of interest (ROIs) with ring artifacts, convert them to polar coordinates, and identify homogeneous rows using a sliding window and signal variance. They then create artifact templates and correct them by subtracting them from each row of the polar image, followed by conversion back to Cartesian coordinates. Chen et al. [16] apply Independent Component Analysis (ICA) in the polar coordinate system to decompose CT images, use smoothing filters to address noise components, and reconstruct the image by combining ICA components before transforming it back to Cartesian coordinates. Liang et al. [35] propose an iterative method that generates residual images by subtracting smoothed images, filtered with Relative Total Variation (RTV), from the originals in polar coordinates, then removes average artifacts and merges the details back into the original image. Wu et al. [36] develop an iterative ring artifact removal method using Unidirectional Total Variation (UTV) and TV-Stokes filtering. Paleo et al. [19] present methods within the Total Variation and Dictionary Learning frameworks. However, filtering and correction based on polar coordinates may reduce image resolution due to coordinate transformations and interpolation.

Dual-domain iterative methods use sparse constraints on stripe artifacts in the sinogram and smoothness constraints on CT images, combining various regularization terms to establish an optimization function for iterative solving. Yu et al. [20] introduced a ring total variation regularization term to the optimization model to penalize ring artifacts in the image domain. A correcting vector was also developed to address detector malfunctions in the projection domain. The optimization problem was solved using an alternating minimization scheme, where the image was updated through the alternating direction method of multipliers (ADMM), and the correcting vector was adjusted based on the updated image.

Zhu et al. [21] used a dual-domain regularization model to directly correct stripe artifacts in the projection domain by adjusting the compensation coefficients for detector response inconsistencies. They also applied smoothing constraints to the reconstructed image to further correct ring artifacts. However, these methods involve simulating forward and backward projections of X-rays, which is very challenging in practice.

Deep learning-based methods for ring artifact removal offer new strategies from a data-driven perspective, leveraging large datasets with and without artifacts to learn how to remove ring artifacts. These methods have significant potential for development and promising application prospects. Chang et al. [22] proposed a CNN-based method to reduce mixed ring artifacts in CT images by combining information from the image and sinogram domains. The CNN inputs the original and sinogram-corrected images and outputs an artifact-reduced image. Image mutual correlation is then used to fuse the sinogram correction with the CNN output, producing a hybrid corrected image. Liu et al. [23] introduced a low-dose CT ring artifact correction method based on detector shifting and deep learning. During CT scanning, the detector is randomly shifted horizontally at each projection to reduce ring artifacts in the pre-processing stage, converting the artifacts into dispersed noise. Deep learning is then used to denoise the dispersed and statistical noise, achieving ring artifact removal. Zhao et al. [25] framed the ring artifact issue caused by detector pixel response inconsistencies as an "adversarial problem," using a GAN-based image transformation strategy to remove ring artifacts from CT images through generative adversarial loss and custom smoothing loss. Wang et al. [24] employed GANs with unidirectional relative total variation loss, perceptual loss, and adversarial loss to effectively remove ring artifacts. However, the effectiveness of deep learning methods for artifact removal heavily relies on the size and quality of the training dataset. The lack of real ring artifact datasets and the discrepancy between simulated and real data lead to suboptimal artifact removal results.

### III. METHOD

This section will provide a detailed description of the proposed method. By utilizing INR to parameterize the sinogram, we decompose it into two parts: IS and SA. The proposed method framework for parameterizing the projection data and separating IS and SA using INRs is illustrated in Fig. 3.

In this section, defective and non-defective pixels are first labeled. Then, a forward model for the decomposition of IS and RS is established, incorporating effective regularization constraints for their separation. The design of the loss function is also presented, followed by a discussion on the residual compensation strategy and the network model selection.

#### A. Labeling Defective and Non-Defective Pixels

To identify defective pixels, the gradient of the sinogram  $P$  is computed in the angular direction, and its average value is compared to a predefined threshold  $\mu = 1 \times 10^{-6}$ . Pixels with an average gradient value greater than  $\mu$  are designated as non-defective (marked as 1), while others are designated

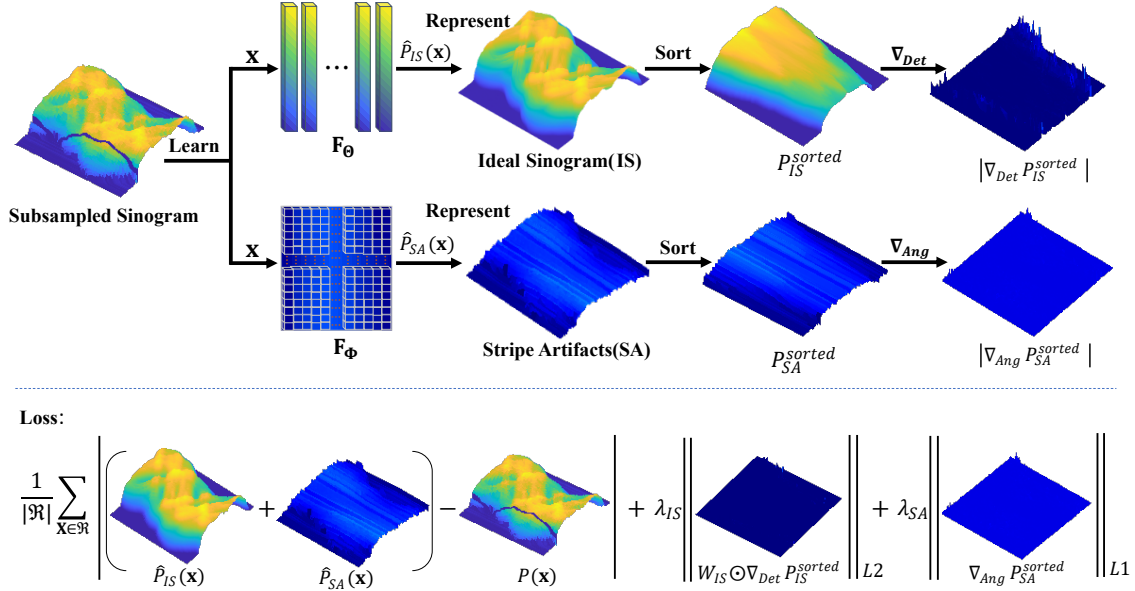


Fig. 3. Framework diagram for the implicit neural representation of sinogram data. The network  $\mathbf{F}_\Theta$  is used to parameterize the IS, while the network  $\mathbf{F}_\Phi$  represents the SA present in the sinogram.  $\mathbf{x}$  denotes the 2D coordinates of the input non-defective pixels.

as defective (marked as 0). The set of non-defective pixels is denoted by  $\mathcal{R}$ , and its indicator function  $\mathbf{I}$  is defined as:

$$\mathbf{I}_{i,j} = \begin{cases} 1, & \overline{\nabla_{Ang} P}_{i,j} > \mu, \\ 0, & \text{otherwise} \end{cases}, \quad (3)$$

where  $i = 1, 2, \dots, M$ ;  $j = 1, 2, \dots, N$ ; here,  $\overline{\nabla_{Ang} P}_{i,j}$  is calculated as:

$$\overline{\nabla_{Ang} P}_{i,j} = \frac{1}{M-1} \sum_{k=1}^{M-1} |P_{k,j} - P_{k+1,j}|,$$

with  $M$  and  $N$  representing the number of view angles and detector bins, respectively.

### B. Implicit Neural Representation of Sinogram Data

Sinogram is modeled as a 2-Dimensional (2D) continuous implicit function  $P(\mathbf{x})$ , which consists of IS  $P_{IS}(\mathbf{x})$  and SA  $P_{SA}(\mathbf{x})$ . For IS and SA, parameterization is performed using networks  $\mathbf{F}_\Theta$  and  $\mathbf{F}_\Phi$ , respectively:

$$\mathbf{F}_\Theta : \mathbf{x} \mapsto P_{IS}(\mathbf{x}), \quad (4)$$

$$\mathbf{F}_\Phi : \mathbf{x} \mapsto P_{SA}(\mathbf{x}), \quad (5)$$

where  $\mathbf{x} = (x, y)$  represents the 2D coordinates of the sinogram. The optimization model proposed in this work consists of two parts that are added together:

$$P_{IS}(\mathbf{x}) + P_{SA}(\mathbf{x}) = P(\mathbf{x}). \quad (6)$$

To ensure the effective parameterization of IS and SA by the networks  $\mathbf{F}_\Theta$  and  $\mathbf{F}_\Phi$ , two unidirectional gradient regularization terms are introduced. A local smoothness term  $\Psi_{IS}$  is applied along the detector direction for  $P_{IS}$ , while a sparsity constraint term  $\Psi_{SA}$  is enforced along the angular direction for  $P_{SA}$ .

To prevent excessive smoothing at IS boundaries, the gradient of the sorted IS  $P_{IS}^{sorted}$  in the detector direction is weighted by the normalized IS values and constrained using an  $L_2$  norm. The local smoothness term  $\Psi_{IS}$  is defined as:

$$\Psi_{IS}(P_{IS}) = \left\| W_{IS} \odot \nabla_{Det} P_{IS}^{sorted} \right\|_2, \quad (7)$$

where  $\odot$  denotes element-wise multiplication. The gradient of  $P_{IS}^{sorted}$  in the detector direction is:

$$\nabla_{Det} P_{IS}^{sorted}{}_{i,j} = \begin{cases} P_{IS}^{sorted}{}_{i,j} - P_{IS}^{sorted}{}_{i+1,j}, & i = 1, \dots, M-1 \\ P_{IS}^{sorted}{}_{i,j} - P_{IS}^{sorted}{}_{1,j}, & i = M \end{cases}.$$

The weighting coefficient is:

$$W_{IS,i,j} = P_{IS,i,j}^{sorted} / \max(P_{IS}^{sorted}).$$

The sparsity constraint term  $\Psi_{SA}$  is given by:

$$\Psi_{SA}(P_{SA}) = \left\| \nabla_{Ang} \hat{P}_{SA}^{sorted} \right\|_1, \quad (8)$$

where the gradient of sorted SA  $P_{SA}^{sorted}$  in the angular direction is given by

$$\nabla_{Ang} P_{SA}^{sorted}{}_{i,j} = \begin{cases} P_{SA}^{sorted}{}_{i,j} - P_{SA}^{sorted}{}_{i,j+1}, & j = 1, \dots, N-1 \\ P_{SA}^{sorted}{}_{i,j} - P_{SA}^{sorted}{}_{i,1}, & j = N \end{cases}.$$

By incorporating the unidirectional regularization constraints  $\Psi_{IS}$  and  $\Psi_{SA}$ , the separation of IS and SA within the sinogram is facilitated. Consequently, the loss function in this work comprises the Mean Absolute Error along with these two regularization constraints:

$$\mathcal{L} = \frac{1}{|\mathcal{R}|} \sum_{\mathbf{x} \in \mathcal{R}} \left| \left( \hat{P}_{IS}(\mathbf{x}) + \hat{P}_{SA}(\mathbf{x}) \right) - P(\mathbf{x}) \right| + \lambda_{IS} \cdot \Psi_{IS}(\hat{P}_{IS}) + \lambda_{SA} \cdot \Psi_{SA}(\hat{P}_{SA}), \quad (9)$$

where  $|\mathcal{R}|$  is the number of elements in the dataset,  $\hat{P}_{IS}$  and  $\hat{P}_{SA}$  denote the predicted values for all pixels (both defective and non-defective), and  $\lambda_{IS}$  and  $\lambda_{SA}$  are hyperparameters.



### C. Compensation of Residuals

In addition to the information captured by  $\mathbf{F}_\Theta$  and  $\mathbf{F}_\Phi$  from the sinogram data, there is a small amount of residual information  $E(\mathbf{x})$ , where  $E(\mathbf{x}) = P(\mathbf{x}) - \hat{P}_{IS}(\mathbf{x}) - \hat{P}_{SA}(\mathbf{x})$ . Since  $E(\mathbf{x})$  contains a small amount of structural information about the reconstructed object, it can be compensated into the output  $P_{IS}^{out}$  to ensure image clarity. The compensation method is defined as:

$$P_{IS}^{out}(\mathbf{x}) = \hat{P}_{IS}(\mathbf{x}) + \kappa \cdot \hat{P}_{IS}(\mathbf{x}) \cdot \tilde{E}(\mathbf{x}), \quad (10)$$

where  $\mathbf{x}$  represents the coordinates of non-defective pixels,  $\kappa$  is the compensation coefficient,  $\tilde{E}(\mathbf{x})$  is the residual information after subtracting its mean value in the angular direction, and  $\hat{P}_{IS}(\mathbf{x})$  is the IS predicted by the trained network  $\mathbf{F}_\Theta$ .

Subtracting the mean in the angular direction removes most stripe noise from  $E(\mathbf{x})$ , leaving only the structural information of the object in  $\tilde{E}(\mathbf{x})$ . The small amplitude of  $\tilde{E}(\mathbf{x})$  is amplified by multiplying it with  $\hat{P}_{IS}(\mathbf{x})$ , enhancing the structural details in proportion to the projection values of  $\hat{P}_{IS}(\mathbf{x})$ , thereby improving image clarity. The parameter  $\kappa$  adjusts the compensation intensity to enhance structure while minimizing noise and distortion.

### D. Network Model

This paper requires two INR models to represent SA and IS separately. The core idea of INR [27]–[30] is to train multi-layer perceptrons (MLPs) with activation functions to map input coordinates to the desired target values, thus learning continuous mapping functions from discrete data. However, while fully connected networks with positional encoding [27]–[29] can record data information through weights, they are computationally inefficient, take a long time to train, and have limited capacity to express complex signals. Recent research [37]–[40] has explored the possibility of using structured storage of latent features and combining structured feature codes with lightweight MLPs networks, which improves efficiency and expressiveness but weakens the continuous representation of INR.

The priority for network  $\mathbf{F}_\Phi$  is its simplicity and fast convergence, without considering its continuous representation capability. Therefore, the simplest network model, a learnable parameter matrix, is chosen. For the network  $\mathbf{F}_\Theta$ , the goal is to accurately reconstruct IS and predict the projection values of defective pixels. IS primarily exhibits low-frequency components and smoothness. Moreover, an ideal network model should demonstrate fast convergence, insensitivity to initial values, and stability during training. Considering these factors, we compared several network models [27], [37], [40]–[42], ultimately selecting the architecture shown in Fig. 4.

The network model  $\mathbf{F}_\Theta$  consists of two key components: a multi-resolution grid module and an MLPs module. The multi-resolution grid module is a trainable component that includes three layers of grids with resolutions in the  $[M/4, M/2] \times [N/4, N/2]$ . Each grid layer stores two feature vectors that capture details at different scales and effectively predict the projection of defective pixels. Additionally, the MLPs module consists of 3 hidden layers, each using ReLU non-linear

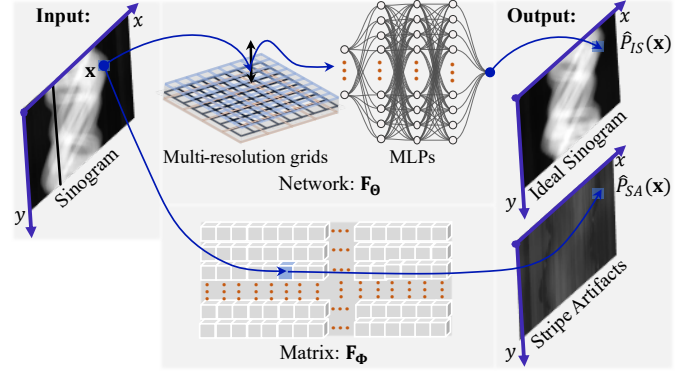


Fig. 4. Network model diagram. The network  $\mathbf{F}_\Theta$  composed of multi-resolution grids and MLPs is used to parameterize IS, while the learnable Matrix network  $\mathbf{F}_\Phi$  represents SA.

activation functions and containing 64 neurons. The network model  $\mathbf{F}_\Phi$  is designed as a learnable parameter matrix with the same resolution as the sinogram with defective pixels removed, where each matrix element is a learnable parameter. Algorithm 1 details the complete process of the proposed method.

---

#### Algorithm 1: Training Details of the Proposed Method

---

**Input** : Sinogram data  $P$ .

**Output**: Corrected Ideal Sinogram  $P_{IS}^{out}$ .

- 1 Establish the coordinate system of  $P$  and normalize its coordinates to the range  $[-1, 1]$ , obtaining the set  $\mathcal{U}$ ;
  - 2 Extract the set of non-defective pixels  $\mathcal{R}$  using (3);
  - 3 Initialize parameters  $\Theta$  for  $\mathbf{F}_\Theta$  and  $\Phi$  for  $\mathbf{F}_\Phi$ ;
  - 4 **for** each training iteration **do**
  - 5     Select a batch  $\mathbf{x}_b$  from  $\mathcal{U}$ ;
  - 6     Compute  $\hat{P}_{IS}(\mathbf{x}_b)$  and  $\hat{P}_{SA}(\mathbf{x}_b)$  using (4) and (5);
  - 7     Extract  $P(\mathbf{x})$ ,  $\hat{P}_{IS}(\mathbf{x})$ , and  $\hat{P}_{SA}(\mathbf{x})$  for  $\mathbf{x} \in \mathcal{R} \cap \mathbf{x}_b$ ;
  - 8     Compute  $\hat{P}_{IS}^{sorted}$  by sorting  $\hat{P}_{IS}(\mathbf{x}_b)$  along the angular axis and store the sorting index;
  - 9     Compute  $\hat{P}_{SA}^{sorted}$  by applying the sorting index from  $\hat{P}_{IS}^{sorted}$  to  $\hat{P}_{SA}(\mathbf{x}_b)$ ;
  - 10     Compute  $\Psi_{IS}$  using (7) and  $\Psi_{SA}$  using (8);
  - 11     Compute the total loss  $\mathcal{L}$  using  $P(\mathbf{x})$ ,  $\hat{P}_{IS}(\mathbf{x})$ ,  $\hat{P}_{SA}(\mathbf{x})$ ,  $\Psi_{IS}$ , and  $\Psi_{SA}$  with (9);
  - 12     Update parameters:  $\Theta^*, \Phi^* = \arg \min_{\Theta, \Phi} \mathcal{L}$ ;
  - 13 **end**
  - 14 Compute the final  $\hat{P}_{IS}$  using  $\Theta^*$  and (4);
  - 15 Output the corrected  $P_{IS}^{out}$  using (10).
- 

## IV. EXPERIMENTS

This section provides a comprehensive evaluation of the proposed method using both simulated and real data. Additionally, experiments are conducted to analyze the effects of different regularization terms.

To ensure a thorough and fair comparison, the proposed method, which is unsupervised and does not require a dataset, is compared with normalization-based methods [14], [43], regularization-based methods [44], W-FFT-based methods [12], FFT-based methods [11], and combined methods

[14]. Furthermore, for real PCD data, the proposed method is compared with those described in [34] and [21].

The PyTorch framework is used to implement the network models. The multi-resolution grid module of network  $F_{\Theta}$  and network  $F_{\Phi}$  are initialized with uniform distributions in the range of  $\pm 1 \times 10^{-4}$  to promote training stability. During training, we use the Adam [45] optimizer, and the initial learning rate for both networks is set to  $1 \times 10^{-4}$ . Regularization parameters  $\lambda_{IS}$  and  $\lambda_{SA}$  need to be increased as training iterations increase. In the early stages of training, if the regularization terms are too large, it may cause the projection values of IS and SA to drop rapidly to zero, hindering further network learning. As training progresses, the projection values of IS and SA gradually increase, and the corresponding regularization terms should also increase. During the experiments, the sinogram is normalized before training, and after training, the predicted data from the INR undergoes inverse normalization. All experiments were conducted on an NVIDIA GeForce RTX 3080 GPU with 10GB memory. Unless otherwise specified, the experiments in this section use the following parameters:  $\lambda_{IS}$  and  $\lambda_{SA}$  start at  $1 \times 10^{-4}$  and are gradually increased to  $5 \times 10^{-3}$  and  $1 \times 10^{-3}$ , respectively;  $\kappa$  is set to 1; and training is conducted for 5,000 iterations.

#### A. Experiment with Numerical Simulation

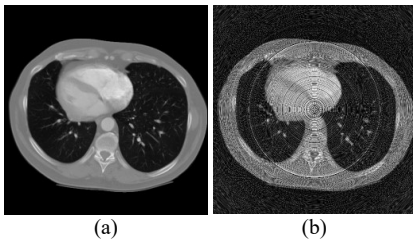


Fig. 5. Simulated phantom. (a) Phantom. (b) Result of FBP [26] from Fig. 6(b). The display range is [0, 0.0015]

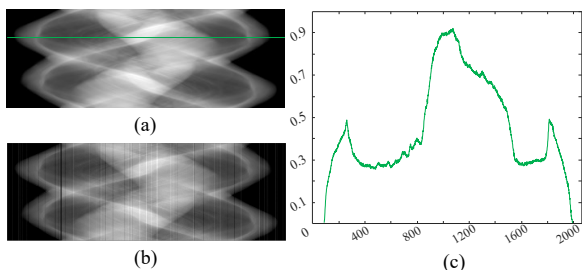


Fig. 6. Simulated sinogram. (a) Sinogram; (b) Sinogram with artifacts; (c) Profile curve of the 200th row in (a).

The phantom in the simulation data is an abdominal CT slice [46]. In the scanning configuration, the distance between the X-ray source and the detector is 416.696 mm. The detector consists of 2068 bins, each with a length of 0.075 mm. The distance between the X-ray source and the rotation center is 297.143 mm. Uniform sampling is performed at 720 view angles within the  $[0, 2\pi]$  range. The sinogram was generated by simulating fan-beam projection [26], as shown in Fig. 6

(a). According to (1),  $\pm 10\%$  photon fluctuations were added to half of the randomly selected pixels to simulate stripe artifacts, and the projection values in columns 400 to 404 were set to zero to simulate defective pixels. Subsequently, Poisson noise with an intensity of  $1 \times 10^5$  was added in the photon domain, resulting in a sinogram with artifacts, as shown in Fig. 6 (b). The result of Filtered back-projection (FBP) [26] reconstruction using the sinogram with artifacts is displayed in Fig. 5 (b). Fig. 6 (c) shows the profile curve of the 200th row in Fig. 6 (a). For the simulation data experiments, the performance of the methods is quantitatively assessed using the Peak Signal-to-Noise Ratio (PSNR) and Structural Similarity Index (SSIM).

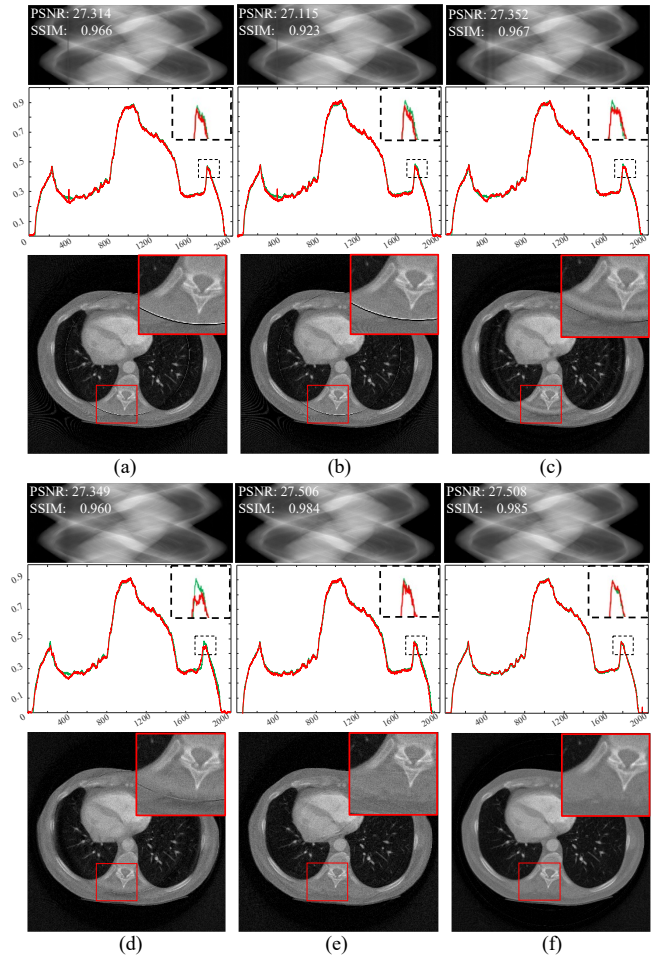


Fig. 7. Comparison experiments with simulated data. (a) Normalization method. (b) Regularization method. (c) W-FFT method. (d) FFT method. (e) Combination method. (f) Proposed method. The display range is [0, 1] for the sinogram and [0, 0.0015] for the CT images.

The experimental results are shown in Fig. 7, which presents the corrected sinograms and provides a quantitative comparison with the reference sinogram regarding PSNR and SSIM. Higher scores indicate better consistency with the reference sinogram. The second row displays the profile curves of the 200th row, with the green curve representing the reference profile and the red curve showing the predicted profile. The third row shows the reconstructed images and their local zoom-in views.

Zoom-in views (a) to (d) in Fig. 7 reveal some ring artifacts, indicating limitations in suppressing defective pixels with these methods. In contrast, the zoom-in views in Fig. 7 (e) and Fig. 7 (f) show reduced ring artifacts, with Fig. 7 (f) exhibiting the least. The image in Fig. 7 (e) presents other types of artifacts. In the profile curves of the 200th row, Fig. 7 (a) to Fig. 7 (d) show noticeable deviations from the reference profile curve in columns 400 to 404. The quantitative evaluation results indicate that the PSNR value of the predicted IS in Fig. 7 (f) performs best among all compared methods, suggesting an advantage in signal fidelity and the suppression of stripe artifacts. Quantitative evaluation results indicate that the SSIM value of Fig. 7 (f) is the highest among all the compared images, demonstrating that this method offers significant advantages in signal fidelity and noise suppression.

In summary, the proposed method performs well in suppressing stripe artifacts and accurately estimating the IS values of defective pixels, thereby improving the quality of image reconstruction to a certain extent.

## B. Experiment with Real Data

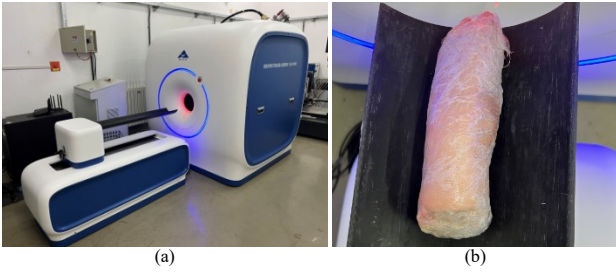


Fig. 8. The experimental PCD-CT system platform and the scanned sample. (a) PCD-CT system platform. (b) Scanned fresh pork trotter sample.

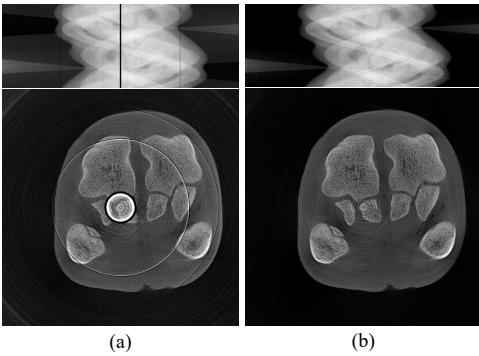


Fig. 9. Real data and FBP [26] results. (a) Unprocessed sinogram and its CT image. (b) Sinogram with black gaps removed using linear interpolation and its CT image. The display range is  $[0, 3.144]$  for the sinograms and  $[0, 0.010]$  for the CT images.

The real data experiment was conducted using a 120 kV X-ray source (Libra13UINE, iRay, China) to generate X-rays. The detector used was a Flat-Panel Photon Counting Detector (EIGER2, DECTRIS, Switzerland). The scanned sample was a fresh pork trotter. Fig. 8 shows the PCD-CT system and the scanned sample. The scanning configuration was consistent with that of the simulated data experiments. Fig. 9 shows the

sinogram data collected during the experiment. The first row of Fig. 9 (a) shows the reference sinogram, where black stripes caused by the gaps between the FPCD panels can be observed. Most existing stripe artifact removal methods struggle to handle artifacts caused by defective pixels, such as these black gaps. To comprehensively evaluate the performance of the proposed method, linear interpolation was used to preprocess these black gaps to evaluate the performance of the proposed method comprehensively. The first row of Fig. 9 (b) shows the preprocessed sinogram. To ensure fairness in the comparison experiments, the relevant parameters of the compared methods were fine-tuned from their default settings to achieve optimal stripe artifact removal performance.

Figures 10 (a), (b), (c), and (h) show the results of stripe artifact removal from the sinogram containing black gaps in Fig. 9 (a). All methods successfully removed the black stripes and reduced other stripe artifacts. The results of the combination method [14] in Fig. 10 (a) demonstrate its effectiveness in removing stripe artifacts. The overall image is clear, and details are well-preserved. However, in the local zoomed-in regions, some ring artifacts remain. Fig. 10 (b) shows the result after applying flat-field correction and linear interpolation for defective pixels (black gaps), followed by TV- $L_1$  aG filtering. The results indicate that while details are well preserved, noticeable ring artifacts remain in the local zoomed-in regions. Fig. 10 (c) uses a dual-domain regularization iterative method. The reconstructed results still show slight ring artifacts in the local zoomed-in regions. Fig. 10 (h) presents the results of the proposed method, where defective pixels (those at the black gaps) were not involved in the neural network training. These defective pixel values were predicted by the network  $\mathbf{F}_{\Theta}$ . The proposed method can maintain image continuity while filling gaps and effectively controlling ring artifacts. Figures 10 (d) to (g) show the experiments on stripe artifact removal from the sinogram after linear interpolation of the black gaps in Fig. 9 (b). Although these methods improved the quality of the reconstructed images and reduced ring artifacts to some extent, residual ring artifacts can still be observed in the local zoomed-in regions. The proposed method in Fig. 10 (f) best preserves image continuity and reduces ring artifacts.

In summary, when comparing the methods in Fig. 10, the method in Fig. 10 (a) is relatively complex, achieving good stripe artifact removal results but still leaving slight ring artifacts. The methods in Fig. 10 (b) and Fig. 10 (c) require extensive parameter tuning to achieve satisfactory results. Methods in Fig. 10 (d) to Fig. 10 (g) leave some residual ring artifacts. Fig. 10 (h) provides the best ring artifact removal and the clearest reconstructed image. Comparative analysis shows that the proposed method effectively removes ring artifacts, whereas other methods leave varying degrees of ring traces in the reconstructed images.

## C. Verification of Regularization Terms

To verify the effectiveness of the two unidirectional gradient constraints and their role in removing ring artifacts from CT images through the sorted sinogram, we used the simulated sinogram shown in Fig. 6 (b). Fig. 11 presents the results obtained by applying different unidirectional gradient constraints



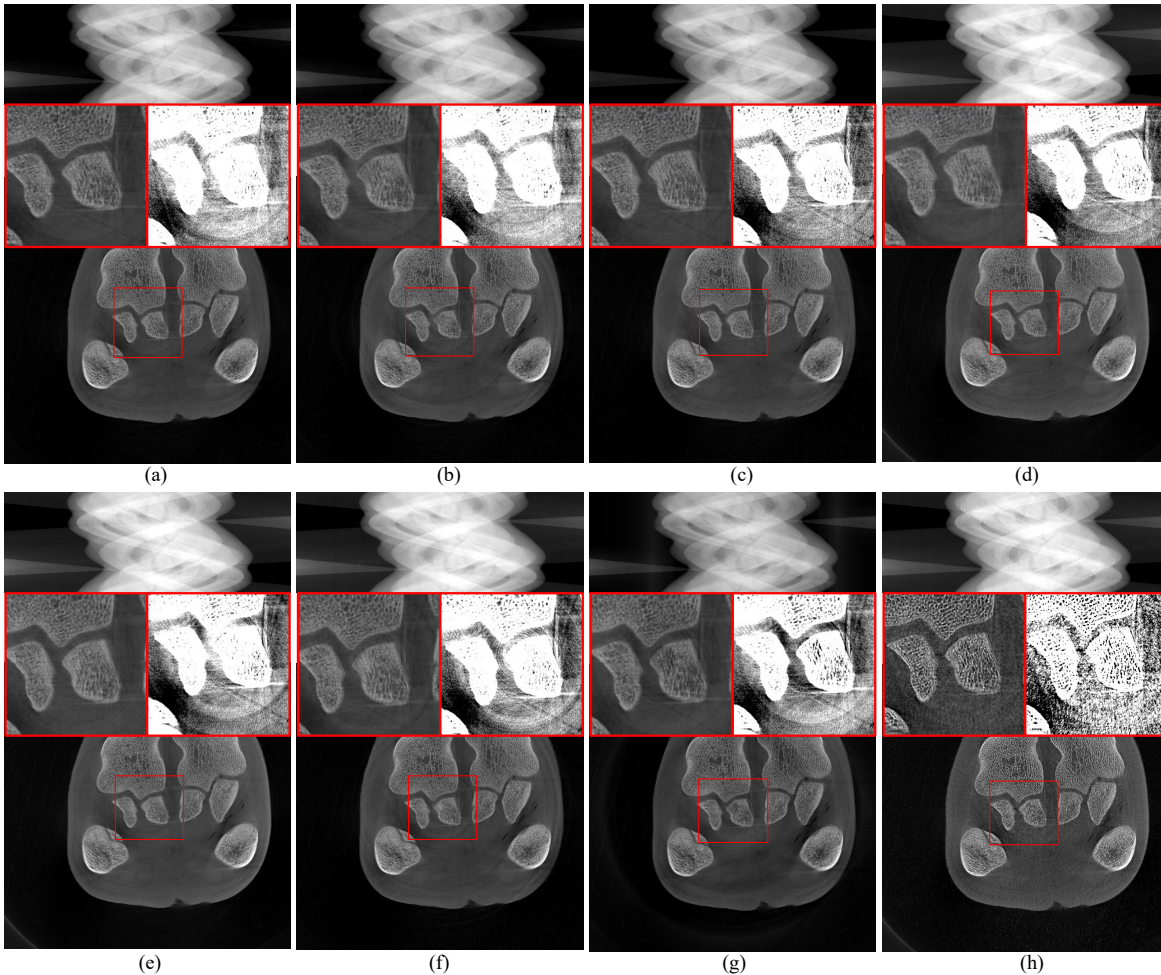


Fig. 10. Comparison experiments with real data. (a) Combination method. (b) Method from [34]. (c) Method from [21]. (d) Normalization method. (e) FFT method. (f) W-FFT method. (g) Regularization method. (h) Proposed method. The display range is  $[0, 3.144]$  for the sinograms and  $[0, 0.010]$  for the CT images. The zoom-in view on the left shows  $[0, 0.010]$ , and on the right, it shows  $[0.0016, 0.003]$ .

to INR, with the number of training iterations fixed at 10,000. The first rows of Fig. 11 show the INR-parameterized IS, respectively, with PSNR and SSIM scores annotated in the figures. The second rows display the profile lines of the 200th row. The green lines represent the reference profile, while the red lines represent the profile lines of the INR-parameterized IS.

From the observations in Fig. 11 (a) and Fig. 11 (b), it is clear that the IS shown in Fig. 11 (a) exhibits significant stripe artifacts. However, the IS of Fig. 11 (b) shows less prominent stripe artifacts, although the profile plot reveals that the IS profile is overly smooth. This indicates that applying only the angular direction gradient  $L_1$  constraint on the SA is insufficient for effectively removing stripe artifacts. Adding a gradient  $L_2$  constraint in the detector direction on the IS can somewhat reduce stripe artifacts, but may also lead to overly smooth images. Further observation of Fig. 11 (c) and Fig. 11 (d) shows that all neural network parameterized IS effectively mitigate stripe artifacts. However, the quantitative metrics indicate that the PSNR and SSIM of Fig. 11 (d) are higher than those of Fig. 11 (c), demonstrating the effectiveness of the detector-direction gradient weighting strategy. In contrast,

the profile lines of Fig. 11 (e) in columns 200 and 1800 do not effectively match the reference profile. In comparison, the IS profile of Fig. 11 (d) more closely aligns with the reference profile. This suggests that applying a weighted gradient  $L_2$  constraint in the detector direction on the sorted IS effectively removes stripe artifacts while maintaining image edge sharpness. Comparing Fig. 7 (f) and Fig. 11 (d) reveals that the use of the residual compensation strategy further enhances the PSNR.

## V. DISCUSSIONS

The experimental results demonstrate that the proposed method performs better than existing methods regarding image clarity, continuity, and ring artifact removal. This section discusses the strengths and limitations of the proposed method.

Regarding image clarity, as shown in Fig. 10, the proposed method produces the clearest reconstructed images. This can be attributed to the effective separation of IS and SA, as well as the compensation of residuals. The residual compensation plays a role in enhancing image details and contrast. Regarding image continuity, as illustrated in Fig. 7, the proposed method



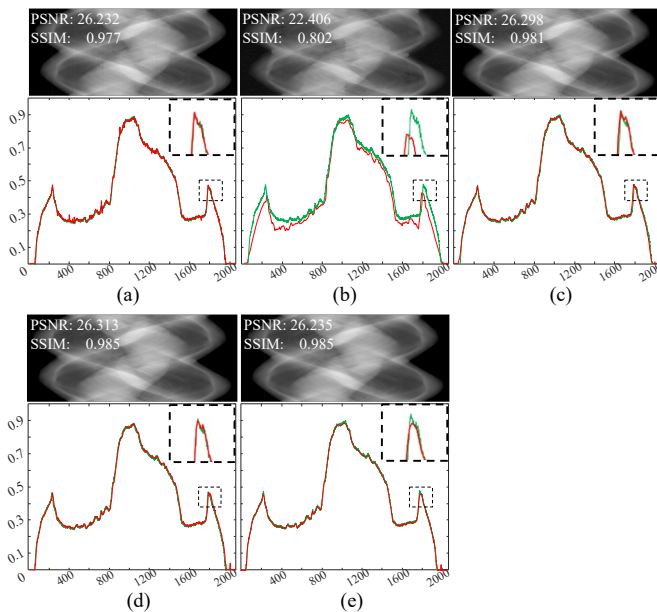


**Fig. 11.** Impact of unidirectional gradient constraints on INR-parameterized IS: (a) Angular gradient with  $L_1$  constraint applied to SA only; (b) Detector gradient with  $L_2$  constraint applied to IS only; (c) Combined angular gradient with  $L_1$  constraint on SA and detector gradient with  $L_2$  constraint on IS; (d) Combined angular gradient with  $L_1$  constraint on SA and weighted detector gradient with  $L_2$  constraint on IS; (e) Unsorted IS and SA with combined angular gradient and  $L_1$  constraint on SA and detector gradient with  $L_2$  constraint on IS. The disparity range is set to  $[0, 1]$ .

successfully predicts the IS values for gaps caused by non-responsive black stripes using the continuous representation capabilities of the implicit neural network. As a result, no residual rings caused by these gaps are visible in the reconstructed images. Both simulation and real data experiments show that the proposed method results in the least residual ring artifacts.

Despite its excellent performance, the proposed method has some limitations. While effective in separating SA from IS, the unidirectional gradient regularization framework may lead to information loss, including minor stripe artifacts and small structural details of the object. A compensation scheme is proposed in (10) to address this limitation. While this scheme is simple and effective in enhancing image clarity and contrast, it does introduce slight stripe artifacts. Future research could explore more sophisticated iterative schemes to incrementally incorporate residual information into the SA, aiming to extract non-stripe information more comprehensively while preserving structural details.

## VI. CONCLUSION

This study proposed a method for effectively separating stripe artifacts from the sinogram using INR parameterization. Applying unidirectional gradient regularization to the SA and IS effectively separated the two. The  $L_1$  regularization of the gradient in the angular dimension enhances the stripe artifact features, while the  $L_2$  regularization of the weighted gradient in the detector direction preserves the local smoothness of the data. Additionally, by utilizing the continuous representation

capability of INR, the proposed method predicts defective pixel projection values using only the inconsistent detector response to X-ray, without requiring additional input. The experimental results demonstrate the effectiveness of the technique in removing ring artifacts from CT images. As a novel ring artifact removal technique, this INR parameterization strategy successfully demonstrates its effectiveness in enhancing CT image quality, providing a new perspective for addressing the challenge of ring artifacts.

## REFERENCES

- [1] J. Hsieh, "Computed tomography: principles, design, artifacts, and recent advances," 2015. [Online]. Available: <https://api.semanticscholar.org/CorpusID:108848922>
- [2] F. E. Boas, D. Fleischmann *et al.*, "Ct artifacts: causes and reduction techniques," *Imaging Med*, vol. 4, no. 2, pp. 229–240, 2012.
- [3] M. Danielsson, M. Persson, and M. Sjölin, "Photon-counting x-ray detectors for ct," *Physics in Medicine & Biology*, vol. 66, no. 3, p. 03TR01, 2021.
- [4] Y. Nakamura, T. Higaki, S. Kondo, I. Kawashita, I. Takahashi, and K. Awai, "An introduction to photon-counting detector ct (pcd ct) for radiologists," *Japanese journal of radiology*, vol. 41, no. 3, pp. 266–282, 2023.
- [5] V. Van Nieuwenhove, J. De Beenhouwer, F. De Carlo, L. Mancini, F. Marone, and J. Sijbers, "Dynamic intensity normalization using eigen flat fields in x-ray imaging," *Optics express*, vol. 23, no. 21, pp. 27975–27989, 2015.
- [6] J. Lifton and T. Liu, "Ring artefact reduction via multi-point piecewise linear flat field correction for x-ray computed tomography," *Optics Express*, vol. 27, no. 3, pp. 3217–3228, 2019.
- [7] L. C. Croton, G. Ruben, K. S. Morgan, D. M. Paganin, and M. J. Kitchen, "Ring artifact suppression in x-ray computed tomography using a simple, pixel-wise response correction," *Optics express*, vol. 27, no. 10, pp. 14231–14245, 2019.
- [8] M. Boin and A. Haibel, "Compensation of ring artefacts in synchrotron tomographic images," *Opt. Express*, vol. 14, no. 25, pp. 12071–12075, Dec 2006. [Online]. Available: <https://opg.optica.org/oe/abstract.cfm?URI=oe-14-25-12071>
- [9] G. Kowalski, "Suppression of ring artefacts in ct fan-beam scanners," *IEEE Transactions on nuclear science*, vol. 25, no. 5, pp. 1111–1116, 1978.
- [10] A. Ashrafuzzaman, S. Y. Lee, and M. K. Hasan, "A self-adaptive approach for the detection and correction of stripes in the sinogram: suppression of ring artifacts in ct imaging," *EURASIP Journal on Advances in Signal Processing*, vol. 2011, pp. 1–13, 2011.
- [11] C. Raven, "Numerical removal of ring artifacts in microtomography," *Review of scientific instruments*, vol. 69, no. 8, pp. 2978–2980, 1998.
- [12] B. Münch, P. Trtik, F. Marone, and M. Stampanoni, "Stripe and ring artifact removal with combined wavelet–fourier filtering," *Optics express*, vol. 17, no. 10, pp. 8567–8591, 2009.
- [13] Y. Mäkinen, S. Marchesini, and A. Foi, "Ring artifact and poisson noise attenuation via volumetric multiscale nonlocal collaborative filtering of spatially correlated noise," *Journal of Synchrotron Radiation*, vol. 29, no. 3, pp. 829–842, 2022.
- [14] N. T. Vo, R. C. Atwood, and M. Drakopoulos, "Superior techniques for eliminating ring artifacts in x-ray micro-tomography," *Opt. Express*, vol. 26, no. 22, pp. 28396–28412, Oct 2018.
- [15] J. Sijbers and A. Postnov, "Reduction of ring artefacts in high resolution micro-ct reconstructions," *Physics in Medicine & Biology*, vol. 49, no. 14, p. N247, 2004.
- [16] Y.-W. Chen, G. Duan, A. Fujita, K. Hirooka, and Y. Ueno, "Ring artifacts reduction in cone-beam ct images based on independent component analysis," in *2009 IEEE Instrumentation and Measurement Technology Conference*. IEEE, 2009, pp. 1734–1737.
- [17] Z. Wei, S. Wiebe, and D. Chapman, "Ring artifacts removal from synchrotron ct image slices," *Journal of Instrumentation*, vol. 8, no. 06, p. C06006, 2013.
- [18] Q. Huo, J. Li, and Y. Lu, "Removing ring artefacts in ct images via unidirectional relative variation model," *Electronics Letters*, vol. 52, no. 22, pp. 1838–1839, 2016.
- [19] P. Paleo and A. Mirone, "Ring artifacts correction in compressed sensing tomographic reconstruction," *Journal of synchrotron radiation*, vol. 22, no. 5, pp. 1268–1278, 2015.

- [20] M. Salehjehromi, Q. Wang, Y. Zhang, L. A. Gjestebj, D. Harrison, G. Wang, P. M. Edic, and H. Yu, "A new iterative algorithm for ring artifact reduction in ct using ring total variation," *Medical physics*, vol. 46, no. 11, pp. 4803–4815, 2019.
- [21] H. Zhu, X. Lu, Y. Qin, X. Yu, T. Sun, and Y. Zhao, "A dual-domain regularization method for ring artifact removal of x-ray ct," *arXiv preprint arXiv:2403.08247*, 2024.
- [22] S. Chang, X. Chen, J. Duan, and X. Mou, "A cnn-based hybrid ring artifact reduction algorithm for ct images," *IEEE Transactions on Radiation and Plasma Medical Sciences*, vol. 5, no. 2, pp. 253–260, 2020.
- [23] Y. Liu, C. Wei, and Q. Xu, "Detector shifting and deep learning based ring artifact correction method for low-dose ct," *Medical Physics*, vol. 50, no. 7, pp. 4308–4324, 2023.
- [24] Z. Wang, J. Li, and M. Enoh, "Removing ring artifacts in cbct images via generative adversarial networks with unidirectional relative total variation loss," *Neural computing and applications*, vol. 31, pp. 5147–5158, 2019.
- [25] S. Zhao, J. Li, and Q. Huo, "Removing ring artifacts in cbct images via generative adversarial network," in *2018 IEEE international conference on acoustics, speech and signal processing (ICASSP)*. IEEE, 2018, pp. 1055–1059.
- [26] A. Biguri, M. Dosanjh, S. Hancock, and M. Soleimani, "Tigre: a matlab-gpu toolbox for cbct image reconstruction," *Biomedical Physics & Engineering Express*, vol. 2, no. 5, p. 055010, sep 2016.
- [27] B. Mildenhall, P. P. Srinivasan, M. Tancik, J. T. Barron, R. Ramamoorthi, and R. Ng, "Nerf: Representing scenes as neural radiance fields for view synthesis," *Communications of the ACM*, vol. 65, no. 1, pp. 99–106, 2021.
- [28] J. T. Barron, B. Mildenhall, M. Tancik, P. Hedman, R. Martin-Brualla, and P. P. Srinivasan, "Mip-nerf: A multiscale representation for anti-aliasing neural radiance fields," in *Proceedings of the IEEE/CVF International Conference on Computer Vision*, 2021, pp. 5855–5864.
- [29] A. Mittal, "Neural radiance fields: Past, present, and future," *arXiv preprint arXiv:2304.10050*, 2023.
- [30] Y. Xie, T. Takikawa, S. Saito, O. Litany, S. Yan, N. Khan, F. Tombari, J. Tompkin, V. Sitzmann, and S. Sridhar, "Neural fields in visual computing and beyond," in *Computer Graphics Forum*. Wiley Online Library, 2022, pp. 641–676.
- [31] Q. Wang, Y. Zhu, and H. Li, "Imaging model for the scintillator and its application to digital radiography image enhancement," *Opt. Express*, vol. 23, no. 26, pp. 33 753–33 776, Dec 2015. [Online]. Available: <https://opg.optica.org/oe/abstract.cfm?URI=oe-23-26-33753>
- [32] Y. Sun, J. Liu, M. Xie, B. Wohlberg, and U. S. Kamilov, "Coil: Coordinate-based internal learning for tomographic imaging," *IEEE Transactions on Computational Imaging*, vol. 7, pp. 1400–1412, 2021.
- [33] G. Zang, R. Idoughi, R. Li, P. Wonka, and W. Heidrich, "Intratomo: self-supervised learning-based tomography via sinogram synthesis and prediction," in *Proceedings of the IEEE/CVF International Conference on Computer Vision*, 2021, pp. 1960–1970.
- [34] K. An, J. Wang, R. Zhou, F. Liu, and W. Wu, "Ring-artifacts removal for photon-counting ct," *Optics Express*, vol. 28, no. 17, pp. 25 180–25 193, 2020.
- [35] X. Liang, Z. Zhang, T. Niu, S. Yu, S. Wu, Z. Li, H. Zhang, and Y. Xie, "Iterative image-domain ring artifact removal in cone-beam ct," *Physics in Medicine & Biology*, vol. 62, no. 13, p. 5276, 2017.
- [36] H. Wu, J. Li, and H. Wang, "Removing ring artifacts in cone-beam ct via tv-stokes and unidirectional total variation model," *Medical physics*, vol. 46, no. 4, pp. 1719–1727, 2019.
- [37] T. Müller, A. Evans, C. Schied, and A. Keller, "Instant neural graphics primitives with a multiresolution hash encoding," *ACM Transactions on Graphics (ToG)*, vol. 41, no. 4, pp. 1–15, 2022.
- [38] A. Chen, Z. Xu, A. Geiger, J. Yu, and H. Su, "Tensorf: Tensorial radiance fields," in *European Conference on Computer Vision*. Springer, 2022, pp. 333–350.
- [39] A. Chen, Z. Xu, X. Wei, S. Tang, H. Su, and A. Geiger, "Factor fields: A unified framework for neural fields and beyond," *arXiv preprint arXiv:2302.01226*, 2023.
- [40] S. Xie, H. Zhu, Z. Liu, Q. Zhang, Y. Zhou, X. Cao, and Z. Ma, "Diner: Disorder-invariant implicit neural representation," in *Proceedings of the IEEE/CVF Conference on Computer Vision and Pattern Recognition*, 2023, pp. 6143–6152.
- [41] V. Sitzmann, J. Martel, A. Bergman, D. Lindell, and G. Wetzstein, "Implicit neural representations with periodic activation functions," *Advances in neural information processing systems*, vol. 33, pp. 7462–7473, 2020.
- [42] R. Fathony, A. K. Sahu, D. Willmott, and J. Z. Kolter, "Multiplicative filter networks," in *International Conference on Learning Representations*, 2020.
- [43] M. Rivers, "Tutorial introduction to x-ray computed microtomography data processing," <http://www.mcs.anl.gov/research/projects/X-ray-cmt/rivers/tutorial.html>, 2024, accessed: 2024-09-11.
- [44] S. Titarenko, P. J. Withers, and A. Yagola, "An analytical formula for ring artefact suppression in x-ray tomography," *Applied Mathematics Letters*, vol. 23, no. 12, pp. 1489–1495, 2010.
- [45] D. P. Kingma and J. Ba, "Adam: A method for stochastic optimization," *arXiv preprint arXiv:1412.6980*, 2014.
- [46] C. McCollough, "Tu-fg-207a-04: overview of the low dose ct grand challenge," *Medical physics*, vol. 43, no. 6Part35, pp. 3759–3760, 2016.